ARTICLE　OPEN

Check for updates

Temporal coherence in particulate matter in East Asian outflow regions: fingerprints of ENSO and Asian dust

Mien-Tze Kueh [ID][1], Chuan-Yao Lin [ID][1 ✉] and Yi-Yun Chien [ID][1]

Understanding temporal coherence in particulate matter (PM) pollution across East Asian outflow regions is crucial for collaborative efforts in addressing air pollution challenges. In this study, we analyze daily PM exceedance patterns using ground-based measurements over the past two decades, focusing on the influence of El Niño-Southern Oscillation (ENSO) and Asian dust activity. ENSO-related coherent PM exceedance shows lower occurrence during El Niño compared to La Niña in spring, due to weakened continental outflows and increased precipitation. Temporal distribution of dust-related coherent PM exceedance closely mirrors springtime dust activity in source regions, indicating significant dust emission impact on outflow regions. Our findings have implications for climate variability and the assessment of multi-decade model simulations.

INTRODUCTION

East Asia is characterized by high levels of particulate matter (PM) emissions[1] and subsequent ambient concentrations[2], which pose significant health and environmental risks. The East Asian ground-level $PM_{2.5}$ (PM with a diameter of 2.5 μm or less) concentrations in wintertime are significantly higher than those in summertime[2]. The $PM_{2.5}$ concentrations exhibit a broad-scale offshore gradient during the cold season from November to April (Fig. 1a). The $PM_{2.5}$ levels are significantly higher over the continental regions compared to the oceanic regions, with the highest values found in northern China. Over the oceanic regions, $PM_{2.5}$ concentrations in South Korea and Taiwan are slightly higher than those in Japan. This eastward diminishing trend of $PM_{2.5}$ levels from coastal China to open waters is also visible from the sparsely distributed ground-based measurements (Fig. 1b, c). This pattern of geographic gradient in particulate levels signifies the impact of transboundary air pollution from the Asian continent[3].

Transboundary air pollution resulting from winter monsoon-driven continental outflows has raised significant environmental concerns in downwind areas such as South Korea[4–7], Japan[3,7–11], Taiwan[12–16], and Hong Kong[14,17–19]. In eastern China, satellite-based estimates of $PM_{2.5}$ show consistent long-term trends with some variations in interannual patterns among subregions (Fig. 1d). The increasing trends of ground-level PM before 2010 can presumably be attributed to the economic growth in China, whereas the decreasing trends from around 2013 have been mainly acknowledged as the efforts of China's stringent emission control measures[20,21]. The seasonal means for the northern and central parts of eastern China have decreased by approximately 30% and 40%, respectively, over the past decade. Notably, the overall reductions in these regions are nearly equivalent to the average $PM_{2.5}$ levels observed in the outflow regions, where the trends, as revealed by satellite estimates, have remained relatively smooth over the years. Ground-based measurements in Taiwan and Hong Kong show reductions of up to 50% in seasonal $PM_{2.5}$ and PM_{10} (PM with a diameter of 10 μm or less) levels over the past two decades, whereas those in Japan and South Korea exhibit less prominent evidence of reduction (Fig. 1e, f). Short-term interannual variations among these regions also exhibit

notable differences, signifying the involvement of distinct underlying mechanisms of ambient PM variability across the outflow regions.

The spatiotemporal variability of PM is shaped by multiple factors, including emission sources, meteorological conditions, atmospheric chemistry, and transport processes. Effective measures aimed at improving air quality can be achieved through emission control policies, and collaborative cross-national efforts are crucial to mitigate air pollution issues across East Asia[9,22]. In recent decades, Japan, South Korea, and Taiwan have experienced a long-term decrease in ambient PM levels, which can be primarily attributed to a significant reduction in domestic anthropogenic emissions; however, transboundary air pollutants still play a significant role in the PM concentrations[9,22–26]. The contribution of meteorological conditions, particularly the weakening of regional wind speeds leading to atmospheric stagnation, can also offset the declining trends in response to the reduction in domestic emissions[9,23,25,26].

Mineral dust, originating from the East Asian arid and semiarid regions, can undergo extensive long-distance transport from these source regions[4,27–29]. The dust outflows exert considerable influence on the downwind regions, with the eastward pathway reaching Korea and Japan[4,5,8,10,11], and the southward pathway extending to Taiwan and Hong Kong[12,14–17]. Over the past four decades, a gradual decrease in the occurrence of springtime Asian dust storms has been observed in the source regions, and primarily attributed to a weakening of surface winds[30–33] and an increase in vegetation coverage[30,32,33]. Short-term variations in surface winds can be ascribed to extratropical cyclone activities[28,34,35], while long-term trends may be linked to large-scale climate variability such as the Arctic Oscillation[28,31,36] and El Niño-Southern Oscillation (ENSO)[31,36,37]. However, the relationship between ENSO conditions and dust activities over the source regions remains inconsistent across previous studies. Notably, the analysis of dust transport pathways over the outflow regions revealed a more southward pathway during La Niña and a more eastward pathway during El Niño[31,36].

There is extensive research examining ENSO's impact on East Asian $PM_{2.5}$ levels, primarily focusing on China[38–41]. Southern and

---

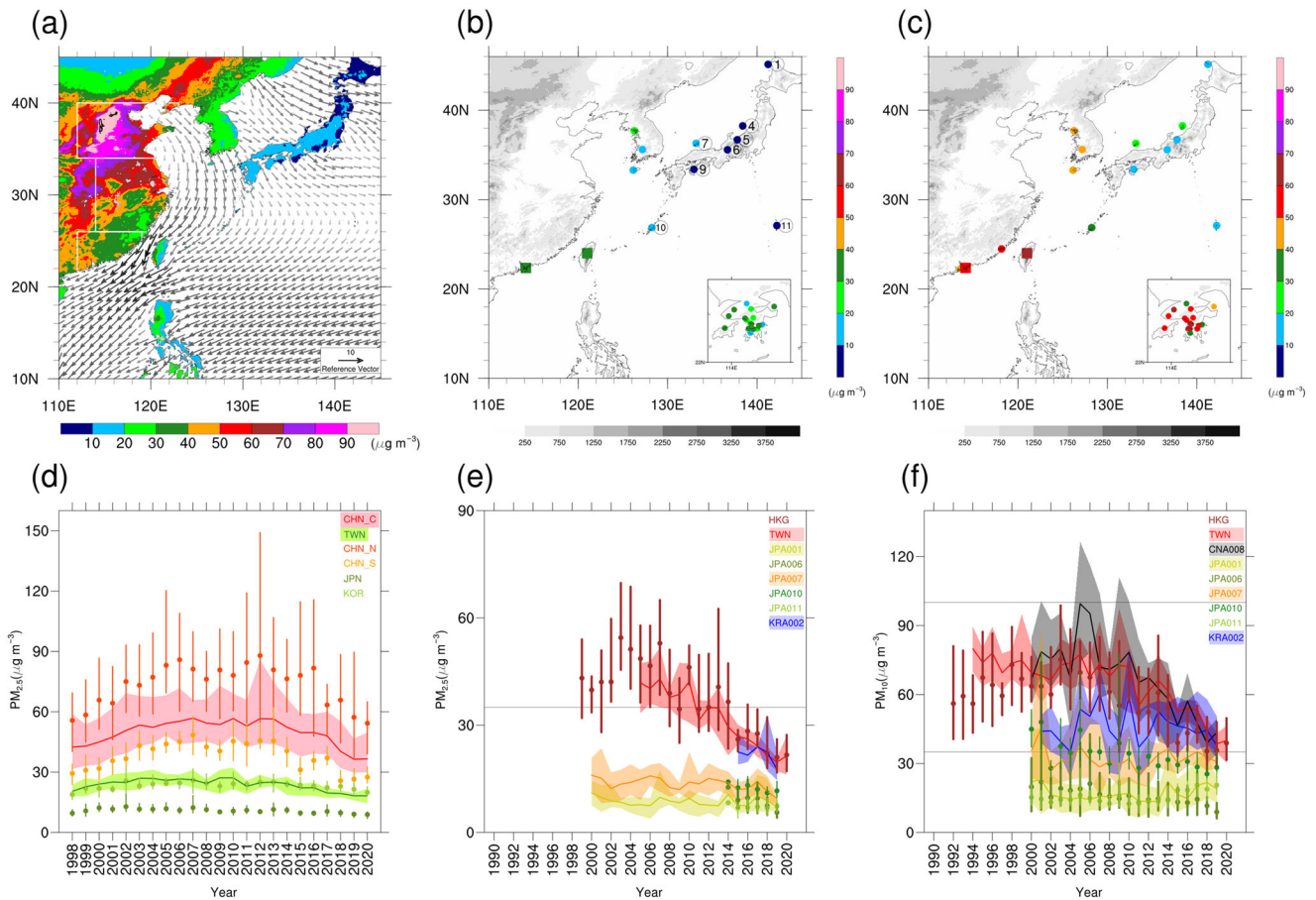[1]Research Center for Environmental Changes, Academia Sinica, Taipei, Taiwan. ✉email: yao435@rcec.sinica.edu.tw

Fig. 1 Long-term averages and variations of ground-level PM concentrations (µg m⁻³) in cold season (November to April). Spatial distributions of **a** satellite-based estimates of PM$_{2.5}$ concentrations and gridded 10 m winds reanalysis, ground-based measurements of **b** PM$_{2.5}$ and **c** PM$_{10}$ concentrations. Concentration time series of **d** satellite-based PM$_{2.5}$, and ground-based **e** PM$_{2.5}$ and **f** PM$_{10}$. In (**b**) and (**c**), dots and squares denote the locations and long-term averages of the ground-based measurements, where dots represent individual sites for Japan and South Korea, and squares represent the means of multiple stations for Taiwan and Hong Kong. The monitoring stations of Hong Kong are presented in the insert maps, those of Taiwan can be found in "Methods". Circled numbers represent the code numbers for Japanese monitoring sites, with their prefix JPA dropped. In (**d**)–(**f**), dots and solid lines denote the means of cold season, whereas vertical bars and shading regions denote the range of cold season (minimum and maximum of monthly values). In (**d**), the continental subregions for the area-averaged time series are bounded by white lines and represent the northern (CHN_N), central (CHN_C), and southern (CHN_S) parts of Eastern China. The oceanic subregions, South Korea (KOR), Japan (JPN), and Taiwan (TWN) are the averages of their respective islands or peninsula. In (**e**) and (**f**), code names represent the ground-based measurements shown in (**b**) and (**c**). Find data sources in "Methods".

Northern China respond differently to ENSO[38–41], attributed to atmospheric changes like precipitation[38,39,41], winds[38–40], and boundary layer height[38]. During El Niño years, higher PM$_{2.5}$ levels in northern China have been associated with enhanced south-easterly winds[39] and a weakened winter monsoon[40]. As northern China is a significant PM source region, applying Chinese research directly to outflow regions without further investigation would bias our understanding. There is limited research on the potential influence of ENSO on ambient PM levels over the East Asian outflow regions. A study investigating ENSO-related PM$_{10}$ variability in South Korea revealed a discernible sub-seasonal pattern, with La Niña years showing higher PM$_{10}$ levels compared to El Niño years[42]. A separate study conducted in Hong Kong showed that both PM$_{2.5}$ and PM$_{10}$ levels had higher seasonal averages in La Niña years compared to El Niño years[19]. These results collectively suggest a significant association between ENSO conditions and PM variations in the outflow regions.

Previous studies have primarily focused on limited geographical areas. Changes in any individual monitoring site can result from various potential causes. By conducting analyses that seek consistent patterns across multiple monitoring sites, it is possible to reduce localized variations and identify influential factors that

have a broad geographical impact. In this article, we use the term "coherence" to describe the consistent and recognizable pattern of PM across the monitoring sites under investigation. For example, coherence may manifest as a consistent tendency of having the same sign over a specific time domain or a recurring occurrence that is consistently more or less frequent under specific conditions. Recognizing the temporal coherence in PM levels across the East Asian outflow regions is crucial for collaborative cross-border efforts to mitigate air pollution issues. Here, we aim to investigate the presence of coherent patterns in the daily PM variations across selected monitoring sites, as depicted in Fig. 1b, in the context of ENSO and Asian dust activity. As the PM levels differ significantly among the sites, standardization of the data is needed for comparison. We use exceedance frequency, which quantifies the occurrence of PM levels exceeding a standardized threshold, as metric for examining coherent patterns ("Methods"). We will demonstrate that conditional sampling based on ENSO phases reveals opposite responses in the terrestrial source region and the outflow regions. In contrast, daily sampling reveals the same tendency in both the terrestrial source region and outflow regions. We will discuss the

RESULTS

Long-term trend and emission

Figure 2 illustrates changes in PM levels relative to 2010. We used a 3-year running average to smooth out significant year-to-year variations in seasonal PM levels to facilitate the comparison of long-term trends. In Taiwan and Hong Kong, there has been a significant 50% reduction in $PM_{2.5}$ levels over the past decade, surpassing the decline in regional $PM_{2.5}$ emissions. In Taiwan, emissions have shown an approximate 80% reduction. However, the long-term trends at the two Japanese sites remain unclear. When examining PM_{10} levels over the past decade, two distinct patterns emerge: a declining one and an increasing one. The declining pattern is more evident, although decline rates differ among sites, generally exceeding those of regional emissions. This consistency between PM levels and emissions is expected since emissions significantly influence PM levels. However, the limitation of using annual regional emissions for Taiwan and Asia in this study greatly hinders our confidence in quantitatively assessing the attribution of site-scale seasonal PM level variations to these emissions. Shifting our focus back to the unsmoothed seasonal PM levels, the pronounced year-to-year variations reveal the influence of other factors. The relatively higher PM levels during 2012–2014 and 2016–2017 in most sites suggest the presence of broad-scale drivers affecting PM levels across the outflow regions. Our attention will be directed toward identifying coherent patterns in temporal domains among study sites rather than examining detailed features at individual sites.

Exceedance frequency and intra-seasonal variation

Figure 3 depicts the temporal variations in the exceedance frequencies of PM at the selected sites. For each site, three sets of exceedance frequencies were calculated using one, two, and three standardized anomalies as thresholds. Notably, these exceedance frequencies exhibit substantial similarity in their temporal patterns. In comparison to monitoring sites in Taiwan, Hong Kong, and China, the Japanese sites consistently demonstrate lower instances of $PM_{2.5}$ and PM_{10} exceedances. In the case of Taiwan and Hong Kong, the temporal variations in the exceedance frequencies using one standardized anomaly (1SD) and the number of stations exceeding the threshold (18 and 8 stations, respectively) show significant resemblance, with their plots almost overlapping. These numbers represent slightly more than half of their respective total number of stations, indicating that the mean values of all stations used for the exceedance calculation are representative of the regions. To ensure an adequate sample for analysis, we consider the exceedance frequencies based on one standardized anomaly for these sites as metrics to identify coherent patterns later on.

There are significant intra-seasonal variations in the frequencies of PM exceedances (Fig. 4). The exceedances at all Japanese sites are noticeably higher during the spring, predominantly from March to April. Conversely, Taiwan and Hong Kong experience higher occurrences of exceedances during the winter. The Chinese coastal site CNA008 exhibits comparable PM_{10} exceedance frequencies in both winter and spring. We conducted additional analyses for the PM exceedance frequencies during winter and spring (Supplementary Figs. 1 and 2), which revealed similar patterns as those highlighted in Fig. 3. The contribution of springtime occurrences to the overall cold season ranges from 70% to 90% for Japanese sites, while for Taiwan and Hong Kong, it ranges from 20% to 40% (Supplementary Fig. 3). Therefore, we anticipate that the temporal coherence we seek primarily emerges during springtime (Fig. 4).

ENSO-related variation

Previous studies have shown that the East Asian winter monsoon (EAWM) weakens and there is excessive precipitation during El Niño, while a reversal of these patterns tends to occur during La Niña[43,44]. Furthermore, these associations between ENSO and EAWM tend to be enhanced during the negative phase of the Pacific Decadal Oscillation (PDO)[45]. Over the past few decades, the PDO has predominantly exhibited a negative phase, the transition began around the winter of 1998/1999 (Fig. 5a). The negative PDO phase has prevailed for the past two decades, with a brief positive phase observed between 2014 and 2016. Notably, during the overall negative PDO phase, there has been an increased frequency of La Niña events. Figure 5b and c show the correlation coefficients of 850-hPa winds and precipitation related to ENSO
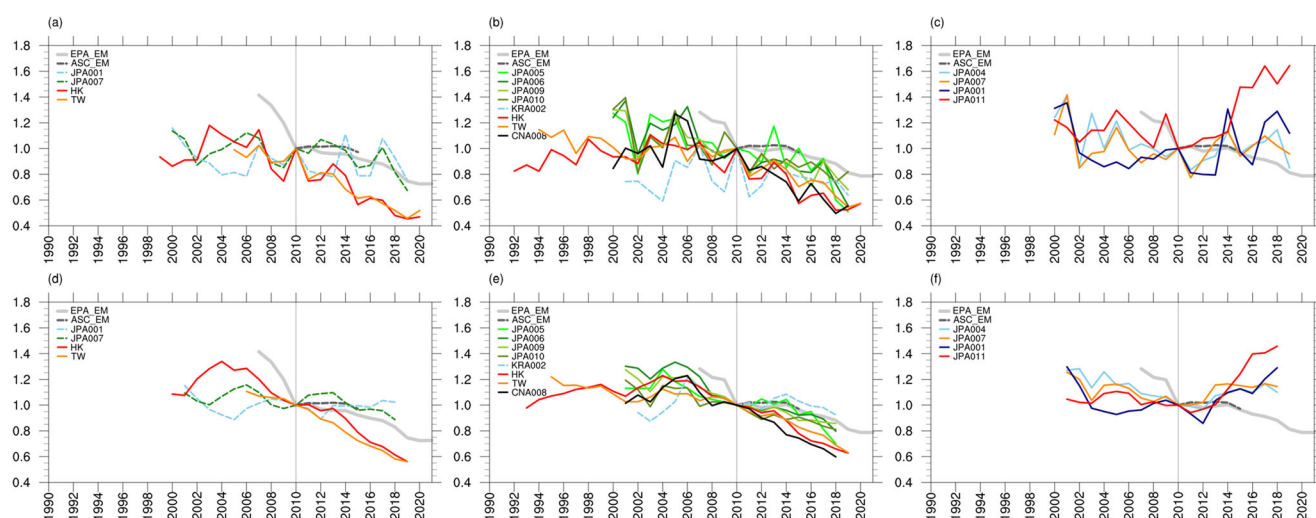

Fig. 2 **Seasonal PM concentrations and annual PM emissions normalized as ratios to the corresponding values in 2010.** The ratios of cold season PM concentrations and annual PM emissions to the corresponding values in 2010 for $PM_{2.5}$ (**a**) and PM_{10} (**b, c**). The ratios of 3-year running averaged cold season PM concentrations and annual PM emissions to the corresponding values in 2010 for $PM_{2.5}$ (**d**) and PM_{10} (**e, f**). The annual PM emissions, EPA_EM and ASC_EM, are the same for $PM_{2.5}$ (**a, d**) and PM_{10} (**b, c, e, f**). EPA_EM (light gray; spanning from 2007 to 2021) and ASC_EM (dark gray dashed; spanning from 2010 to 2015) are emissions from Taiwan and Asia, respectively. The year 2010 is used as a baseline because it is the first year of ASC_EM, derived from AERSv3[1], used in this study.
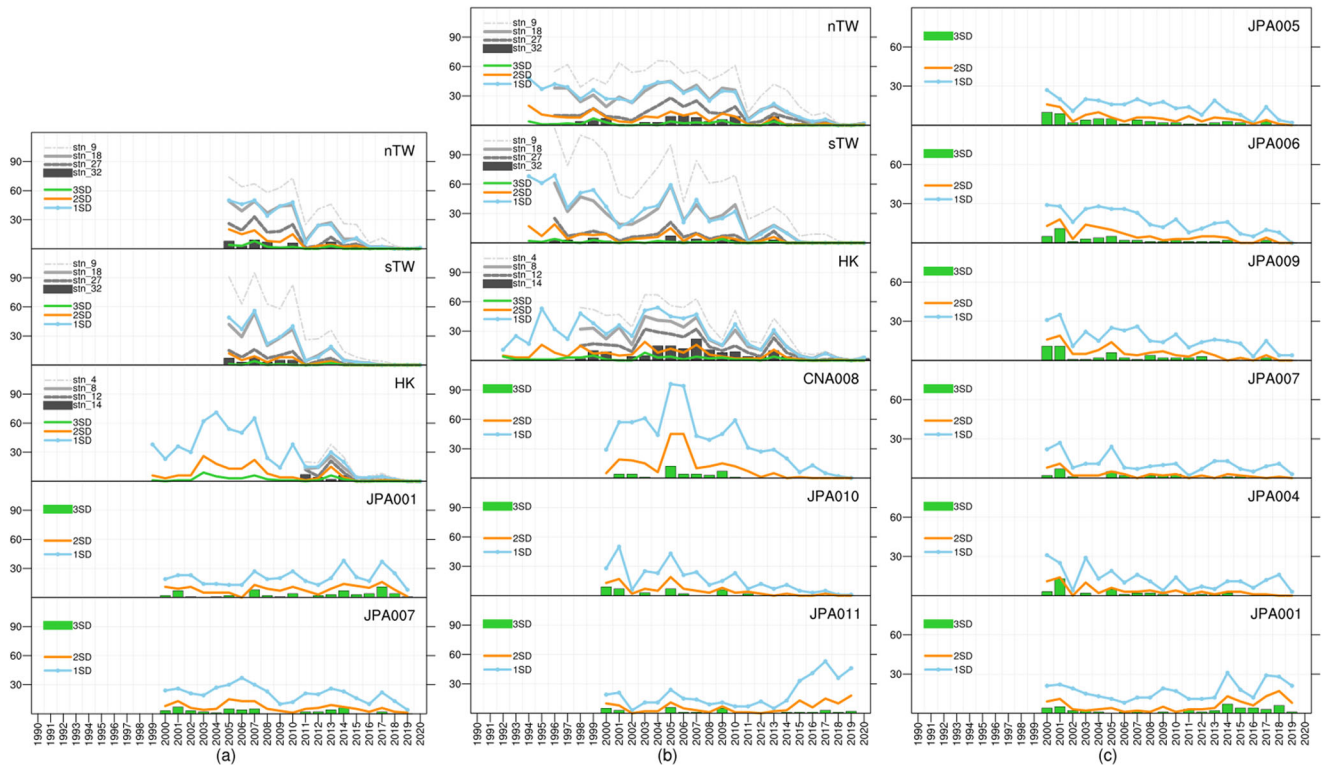
Fig. 3 Temporal variations of daily PM exceedance frequencies. The exceedance frequency of $PM_{2.5}$ (**a**) and PM_{10} (**b**, **c**) derived from ground-based measurements for cold season. Y-axis is numbers of day, X-axis shows the years of the first month in the cold season. Each site has three sets of exceedance frequencies, which employ one, two, and three standardized anomalies as the thresholds for calculation, and are denoted as 1SD, 2SD, and 3SD, respectively. Code names with prefixes JPA and CNA are for Japan and China, respectively. The exceedance frequencies of Taiwan (nTW and sTW) and Hong Kong (HK) were derived from their respective daily mean values of selected stations. For nTW, sTW, and HK, additional sets of exceedance frequency were derived using the numbers of stations exceeding one standardized anomaly (1SD) as thresholds; the legends with prefix stn followed by a number indicate the number of stations used in the concurrence calculation.
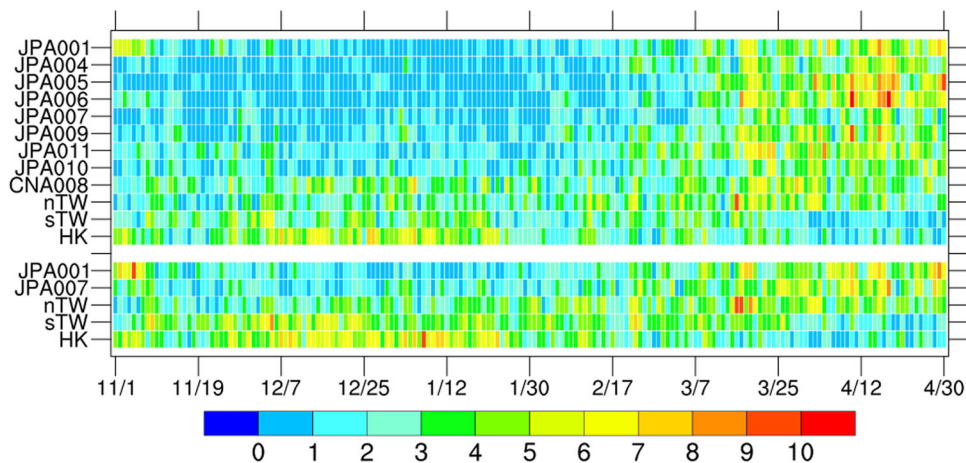

Fig. 4 Intra-seasonal variations of daily PM exceedance frequencies. The density plot of the long-term calendar distribution of PM exceedance frequencies for the selected sites over the period spans from 2000/2001 to 2019/2020 (cold season, from November to April). Each cell on the plot represents the total occurrence of exceedance (units: days) for a specific site on a given calendar day. The Y-axis corresponds to the different sites, while the X-axis represents the calendar days. The four sites in the lower part are for $PM_{2.5}$, whereas the rest are for PM_{10}.

and PDO, respectively. During El Niño (positive phase), anomalous southwesterly and southeasterly winds occur south and north of approximately 30°N, accompanied by positive precipitation anomalies stretching from southern China to southern Japan. These patterns are associated with two anomalous anticyclones situated over the Philippine Sea and the Kuroshio extension, respectively, induced by El Niño as introduced in previous studies[43,44]. During a positive PDO phase, similar but weaker patterns can be observed. The positive precipitation anomalies are associated with positive anomalies in relative humidity, which are centered over Eastern China (Fig. 5d). Across the outflow regions, a broad expanse of negative boundary layer height anomalies, stretching from the northern South China Sea to Japan, is observed during El Niño events (Fig. 5e). These correlation
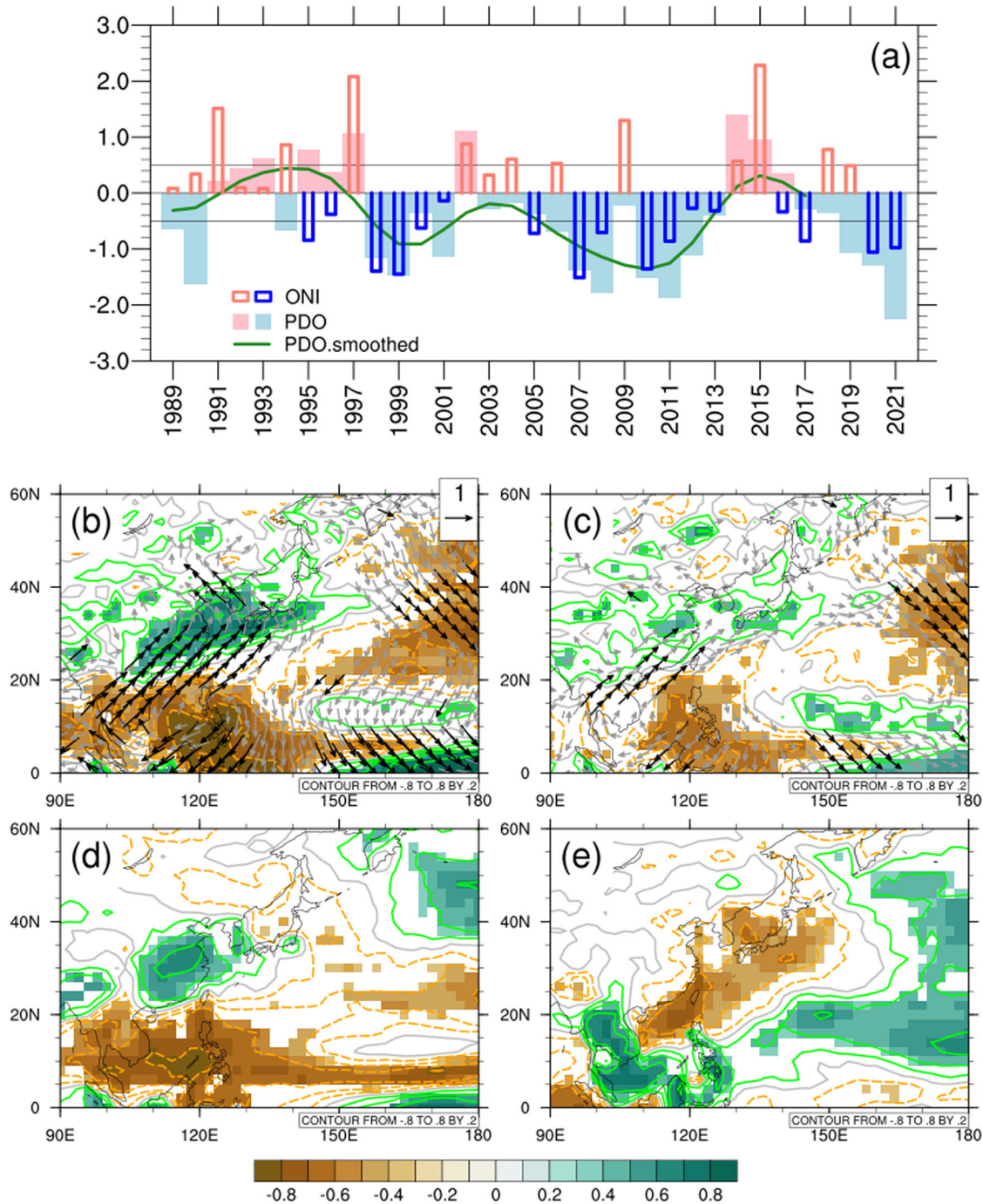
Fig. 5 Temporal variations of ENSO and PDO and their correlations with atmospheric fields. a The temporal variations of Oceanic Niño Index (ONI) and PDO index. The ONI is used as a measure of ENSO; positive for El Niño condition and negative for La Niña condition. PDO.smoothed is the 9-year running-averaged PDO index. *X*-axis shows the years of the first month in the cold season. Correlation coefficients of precipitation (contour and shading) anomalies and wind (vectors) anomalies at 850-hPa with respect to the **b** ONI and **c** PDO index, and correlation coefficients of **d** relative humidity at 850-hPa, and **e** boundary layer height with respect to the ONI. The periods of calculation are 1998–2020 for precipitation, and 1990–2020 for wind, relative humidity and boundary layer height. For scalar fields, shading indicates the region exceeding the 95% confidence level based on the Student's *t*-test. For 850-hPa winds, black vector indicates both wind components exceed the 95% confidence level, gray vector indicates at least one component exceeds the confidence level.

patterns persist throughout both winter and spring (Supplementary Figs. 4 and 5).

However, distinct variations in the correlation patterns of PM$_{2.5}$ in relation to ENSO become evident when comparing winter and spring conditions (Fig. 6). During the winter season, the correlation coefficients of PM$_{2.5}$ exhibit contrasting trends in northern and southern China. South of 30°N, a reduction in PM$_{2.5}$ levels is linked

to El Niño conditions, while north of this latitude, PM$_{2.5}$ concentrations tend to increase. During the spring season, the areas with positive PM$_{2.5}$ anomalies over China notably diminish. However, there is a region of positive PM$_{2.5}$ anomalies that remains over northern East China where the climatological PM$_{2.5}$ concentrations are generally higher than 80 µg m^{-3}, as shown in Fig. 1a. This region can be deemed a significant source area for the
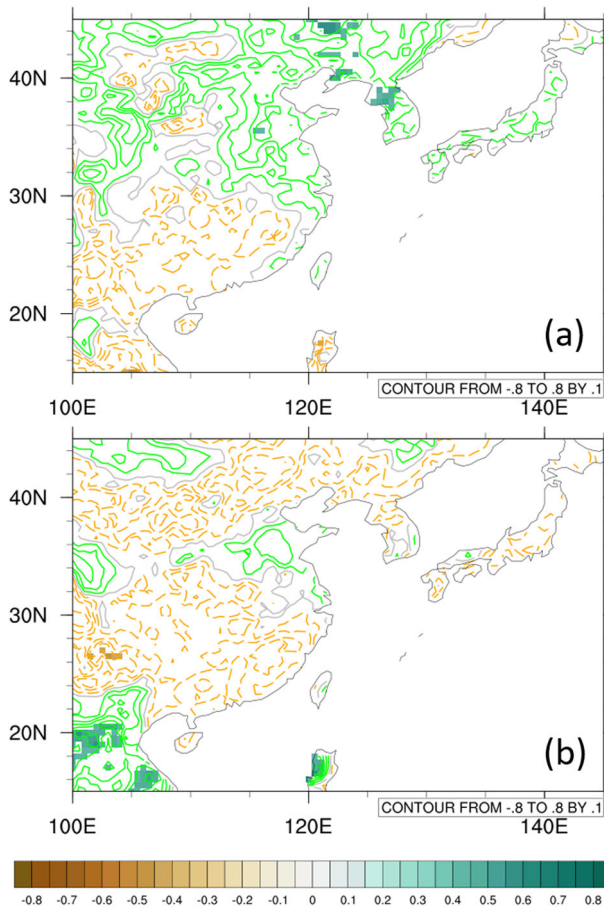
Fig. 6 The correlations of PM$_{2.5}$ concentrations with ONI. Correlation coefficients of satellite-based estimates of PM$_{2.5}$ concentrations (contour and shading) anomalies with respect to the **a** winter (NDJ) and **b** spring (FMA) ONI. The periods of calculation are 1998–2020, shading indicates the region exceeding the 95% confidence level based on the Student's t-test.

surrounding regions. The persistence of positive PM$_{2.5}$ anomalies in this region suggests that the anomalous southeasterly winds during El Niño can impede the dispersion of air pollution, consequently aiding in reducing pollution in the outflow regions. A seasonal variation is also observed in the outflow regions. During the winter season, PM$_{2.5}$ increases are also observed in the outflow regions, specifically South Korea, Japan, and Taiwan. In contrast, negative PM$_{2.5}$ anomalies emerge in the outflow regions during the spring season. Across the continent, the PM$_{2.5}$ correlation coefficients vary from 0.2 to 0.3, lower than atmospheric field correlations (0.4 to 0.6). It is essential to note that, within our domain of interest, these correlation coefficients lack statistical significance, unlike the significance observed for atmospheric variables.

During El Niño conditions, the reduction in PM$_{2.5}$ levels in southern China can be attributed to increased precipitation[38,39,41]. In contrast, the rise in PM$_{2.5}$ levels in northern China has been associated with enhanced surface southeasterly winds[39], a weakened EAWM[40], and a decrease in wind speed and boundary layer height[38]. A positive correlation between relative humidity and PM$_{2.5}$ is suggested for northern China due to the diminished impact of precipitation in the area[41]. However, our findings reveal that northern China is not the primary affected region for both relative humidity and boundary layer height anomalies. Consequently, it is anticipated that during El Niño condition the southerly wind anomalies on the western peripheries of the

anomalous anticyclones contribute to a weakening of the EAWM, subsequently reducing the dispersion of air pollution over the continent. This can lead to a decreased outflow of pollutants from the continent, thereby offsetting the adverse condition of a decreased boundary layer height, which can suppress the vertical dispersion of pollutants over the outflow regions.

From the winter seasons spanning 2000/2001 to 2019/2020, a total of 7 El Niño and 7 La Niña events were identified and analyzed to determine the proportions of PM exceedance at various monitoring sites (Fig. 7). The proportion is the ratio of the number of exceedance days to non-exceedance days for each site during both El Niño and La Niña events ("Methods"). Our findings indicate a consistent decrease in the proportions of PM exceedances at the majority of monitoring sites during El Niño in the spring season. With the exception of the far north Japanese site (JPA001), which demonstrated higher proportions during El Niño. During the winter season, although no visible coherence was observed across the monitoring sites, we emphasize the consistent lower proportions of PM$_{2.5}$ and PM$_{10}$ exceedances in Hong Kong, similar to the findings in spring. Additionally, we note inconsistent patterns in southern Taiwan (sTW), where higher proportions of PM$_{2.5}$ exceedance occurred alongside lower proportions of PM$_{10}$ exceedance.

Overall, our findings support the notion that decreased levels of PM during El Niño in Hong Kong and South Korea can be attributed to weakened continental outflows and increased precipitation[19,42]. In contrast, increased levels of PM during La Niña resulted from enhanced transboundary air pollution and precipitation deficit. Although Wie and Moon's study[42] primarily focused on PM$_{10}$ in South Korea, their investigation of El Niño-related anomalous winds and precipitation encompassed both South Korea and Japan, excluding the far northern region of Japan and the remote eastern islands where monitoring stations JPA001 and JPA011 are located. Therefore, we can apply Wie and Moon's study[42] to interpret the decreased PM exceedance observed in Japanese sites influenced by El Niño. Additionally, we offer possible explanations for the contrasting proportions of PM$_{2.5}$ exceedance during El Niño between winter and spring in southern Taiwan (sTW), which consists of stations in central and southwestern Taiwan ("Methods"), areas prone to local emissions and transboundary air pollution[13,23], as well as unfavorable conditions for pollutant dispersion[23]. Climatologically, this region experiences a dry period from winter to spring, with greater rainfall occurring in spring compared to winter, primarily due to the further southward propagation of frontal precipitation, accompanied by more convective activity in spring[46]. The weakened winter monsoon associated with El Niño can hinder the dispersion of local pollutants in both winter and spring, thus countering the effects of reduced transboundary air pollution. However, we anticipate that El Niño-related excessive precipitation could enhance precipitation scavenging during spring, whereas its influence on winter precipitation is relatively limited. Nevertheless, the wintertime proportion of PM$_{10}$ exceedance remains lower during El Niño, further investigation is necessary to fully understand the contribution of ENSO in the PM exceedance in Taiwan.

East Asian dust activity

The ground-based PM$_{10}$ measurements can be classified into two groups: northern and southern, with a division at 30°N. There are 6 sites in the northern group and another 6 in the southern group (Fig. 3b, c). We conducted a daily analysis to determine the occurrence of PM$_{10}$ exceedance across these monitoring sites. Specifically, we counted the number of days when multiple sites simultaneously exceeded their respective PM$_{10}$ thresholds. This analysis was performed for different combinations of sites, as depicted in Fig. 8a. Notably, we observed the simultaneous
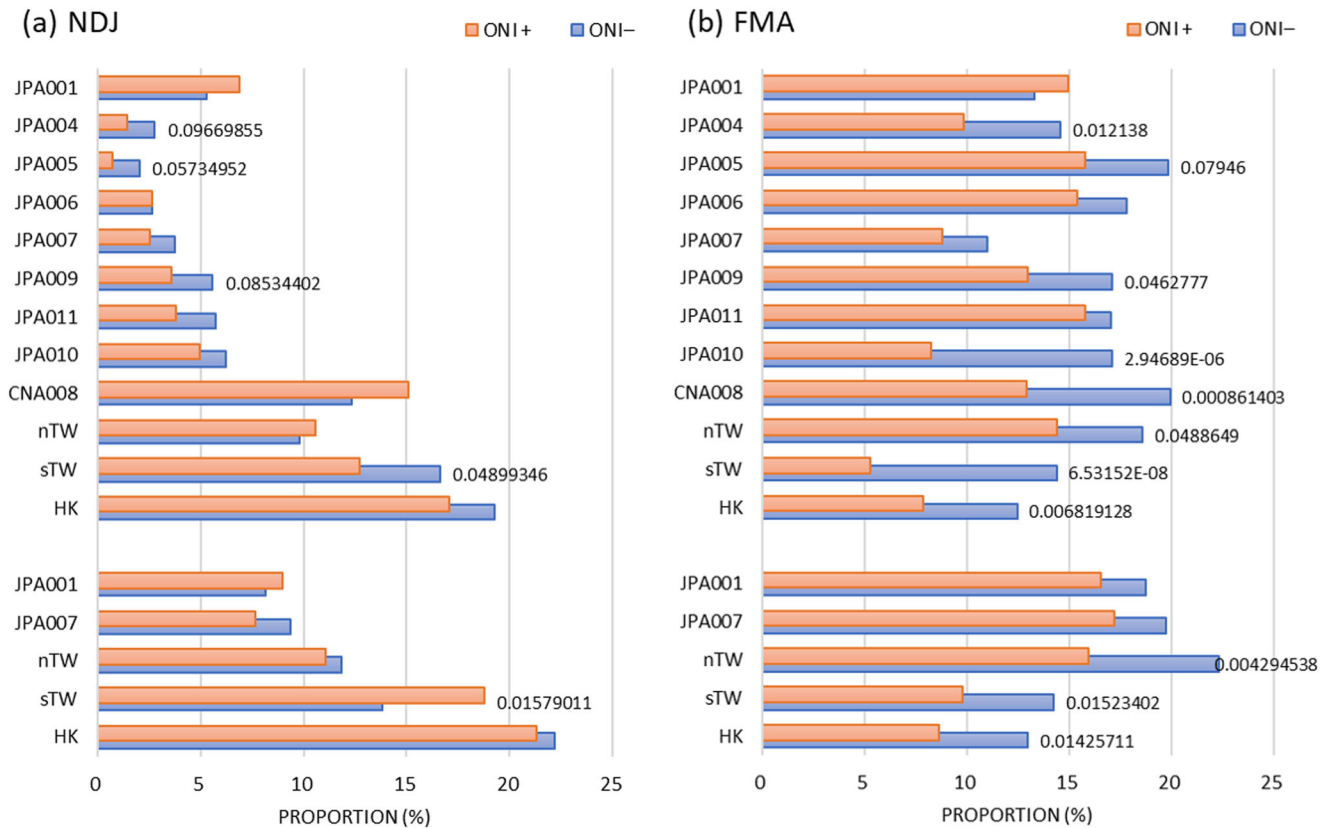
Fig. 7 Proportion of PM exceedances during El Niño and La Niña events. The proportions are calculated as the ratio between the numbers of exceedance and non-exceedance days for **a** Winter (NDJ) and **b** Spring (FMA). Calculation is conducted for the ENSO events listed in "Methods". The numbers alongside the bars correspond to the p-value of the statistical tests for the difference between El Niño and La Niña events; only p-value < 0.05 are shown. The five sites in the lower part are for $PM_{2.5}$, whereas the rest are for PM_{10}.

occurrence of PM_{10} exceedance at all sites within both the northern and southern groups. When considering all 12 sites, there is a noteworthy number of instances where 9 sites simultaneously exceeded their respective thresholds. Consequently, we identified a total of 47 dates exhibiting this concurrence of PM_{10} exceedance across 6, 6, and 9 sites in the northern, southern, and all 12-site groups, respectively. To illustrate the temporal distribution of these dates from 2001 to 2015, we constructed a histogram displayed in Fig. 8b. The temporal distribution reveals a long-term decreasing trend, although significant interannual variations exist. There are 45 out of the 47 dates that occurred before 2011. Notably, the year 2001 recorded the highest number of concurrences. Additionally, there are noticeable peaks in concurrence between 2004 and 2006, as well as between 2008 and 2010.

Taking into account the far-northern site JPA001 in the northern group and the far-eastern site JPA011 in the southern group, Asian dust weather could potentially be a contributing factor to simultaneous exceedances across such a wide geographical area. Therefore, we expected a strong association between the 47 dates under investigation with Asian dust activity. We employed a combination of data from the dust weather visual report and existing literature to ascertain the connection between these dates and dust activity. Specifically, we cross-referenced dates with numbers of dusty grid cells exceeding a specified threshold, termed "dust-related," with previously documented dust event dates in existing literature ("Methods"). The result confirms that 44 out of the 47 dates can be identified as dust-related phenomena, among which 41 dates can be cross-referenced to dust event dates in existing literature. Cross-referencing is a valuable process

in our dust-related date verification, as it helps ensure the reliability of dust-related dates by confirming them from independent research of dust events in the existing literature. As for the remaining 3 dates, we were unable to reach a definitive conclusion. Therefore, the temporal distribution shown in Fig. 8b reveals the Asian dust activity over the outflow regions.

Springtime Asian dust activity in its source regions exhibited a gradual decline from the 1980s to the late 2010s, punctuated by notable peaks in the 2000s, demonstrating a fluctuating yet overall decreasing pattern[30–33]. In our analysis spanning the past two decades (the 2000s and 2010s), the pattern of temporal variations (as shown in Fig. 8b), including the highest occurrences in 2001 and 2002, as well as noticeable peaks in 2004–2006 and 2008–2010, aligns with previous studies that investigated dust storm outbreaks[30], dust storm frequency[32], and dust storm days[33] in the Asian source regions. There is limited research on the long-term trend of spring dust variations over the East Asian outflow regions. Nevertheless, earlier studies in Taiwan[16], Japan[31], and South Korea[47] reported a relatively calm period in the late 1990s followed by a sudden increase in dust frequency in the early 2000s. Additionally, a recent study[48] based on long-term model simulations revealed a similar temporal distribution (as depicted in our Fig. 8b) for spring surface dust frequency in Taiwan and East Asian dust emission. The authors attributed the decline in Taiwan's dust trends to the decreasing Asian dust emissions. Consistent with the existing literature, our findings highlight the significant influence of Asian dust emissions on dust variations over the outflow regions.

We also observed distinct patterns in the dust transport pathways, providing additional insights. By analyzing the
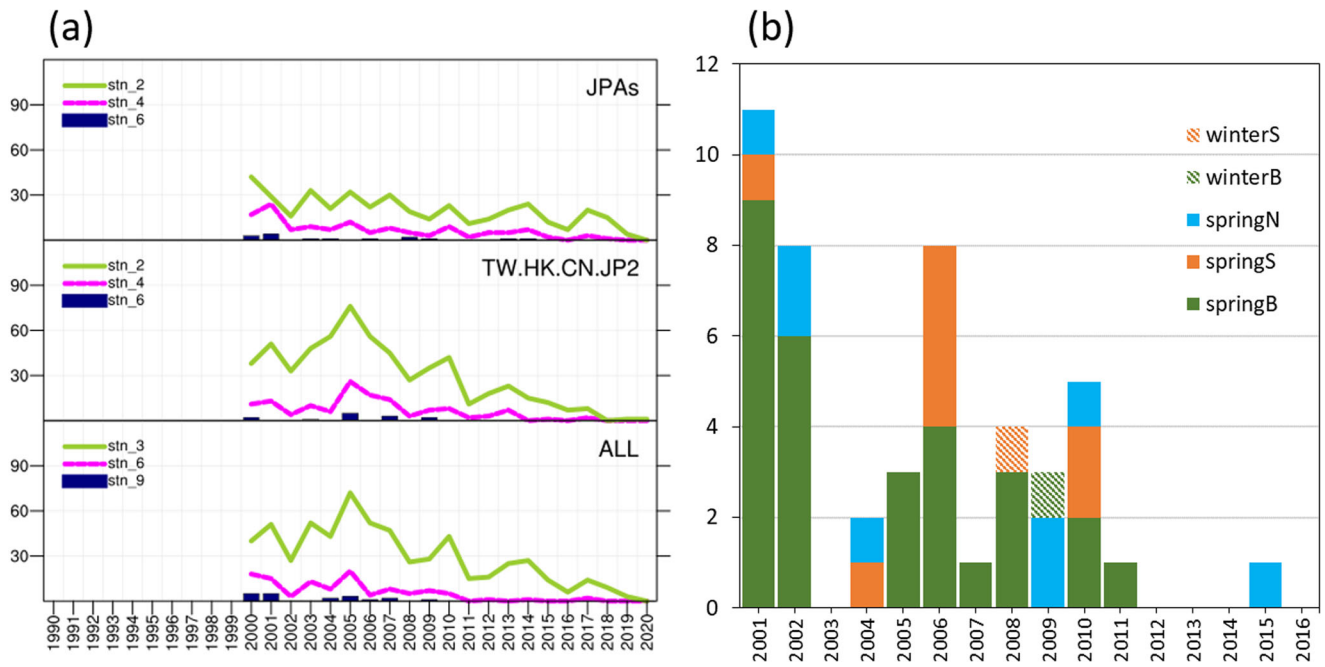
Fig. 8 The concurrence of PM₁₀ exceedance across the sites. a The numbers of days when multiple sites simultaneously exceeded their respective thresholds. *Y*-axis is numbers of day, *X*-axis shows the years of the first month in the cold season. From the top to bottom, panels are for the northern (6 sites), southern (6 sites), and all 12-site groups. The legends with prefix stn followed by a number indicate the number of sites used in the concurrence calculation. **b** The histogram of the 47 dates exhibiting the concurrence across 6, 6, and 9 sites in the northern (N), southern (S), and all 12-site (B) groups, respectively ("Methods"). In the legends, prefixes winter and spring denote the season of the dates. Note that here *X*-axis shows the years of the spring months.

simultaneous occurrence of PM_{10} exceedance among different groups (northern, southern, and all 12-site), we categorized the resulting concurrence dates into three pathways: northern, southern, and broad. Figure 9 shows composite satellite aerosol optical depth (AOD) data for the three pathways, sourced from Moderate Resolution Imaging Spectroradiometer (MODIS) Level 3 products ("Methods"). The northern pathway exhibits higher AOD levels over the seas surrounding Japan, while the southern pathway indicates relatively higher AOD levels over the ocean east of Taiwan. The broad pathway displays intermediate AOD levels between the northern and southern routes. The long-term mean values of area-averaged AOD over the northern and southern continental areas are slightly above 0.4, while they are approximately 0.4 and 0.3, respectively, over the northern and southern oceanic areas. All three pathways exhibit increased AOD levels over continental and oceanic regions compared to the long-term spring season average, as evident in the area average AOD plots. We also present the components of coarse-mode AOD (CAOD) ("Methods"). The CAOD can serve as a proxy for representing the cumulative impact of extinction attributable to coarse particles in the atmosphere[49]. In northern latitudes, the highest CAOD over land is observed in the southern pathway composite, presenting a value of 0.4, which constitutes roughly 64.5% of the total AOD. For the southern pathway, the most distinct feature is the lower CAOD over the northern ocean and higher CAOD over the southern ocean. Overall, the results suggest that Asian dust activity contributes to the simultaneous occurrence of PM_{10} exceedance.

The recirculation accompanying the split high-pressure center in the southern pathway composite contributes to higher AOD levels in the southern oceanic region (Fig. 10). This recirculation can trap near-surface pollutants, preventing their escape and leading to elevated AOD levels in the region. In contrast, easterly winds in the northern and broad pathway composites originate from the far-eastern region, bringing clean air toward the

southern oceanic region and resulting in lower AOD levels there. The configuration of the low-level trough is a key factor that differentiates the northern and southern pathways. In the southern pathway composite, the low-level trough migrates further east, placing Japan and South Korea behind the trough. The trough covers a vast expanse, characterized by surface pressures below 1004 hPa. Conversely, the low-level trough's spatial extent is relatively limited to the west of 150°E, with surface pressures slightly above 1004 hPa in both the northern and broad pathway composites. Japan and South Korea are located in the pre-trough southwesterly flow regimes, primarily coming from northeastern China.

Additionally, we emphasize two dates in our study related to Asian dust events that involved long-range transport to the Arctic in 2010[27] and 2015[29]. Dust events can persist for multiple days, with various dust transport pathways occurring based on the source areas of the dust plume in relation to synoptic conditions[50]. The long-term variations in dust transport pathways across the East Asian outflow regions have yet to be fully investigated. Previous studies on dust transport have predominantly focused on specific events and limited geographical areas[4,5,8,10,11,14–17,27,29,31,36]. Consequently, our sample size is relatively small to draw definitive conclusions. Further investigation is warranted to delve deeper into this topic.

DISCUSSION

This research identified two coherent patterns of PM exceedance in East Asian outflow regions over the past two decades. These patterns are primarily influenced by the ENSO and Asian dust, we consider them as distinct fingerprints of the driving factors' impacts on the PM temporal variability. Here, we discuss the implications of our findings within the framework of (1) climate variability and climate change, and (2) the assessment of multi-decade model simulations.
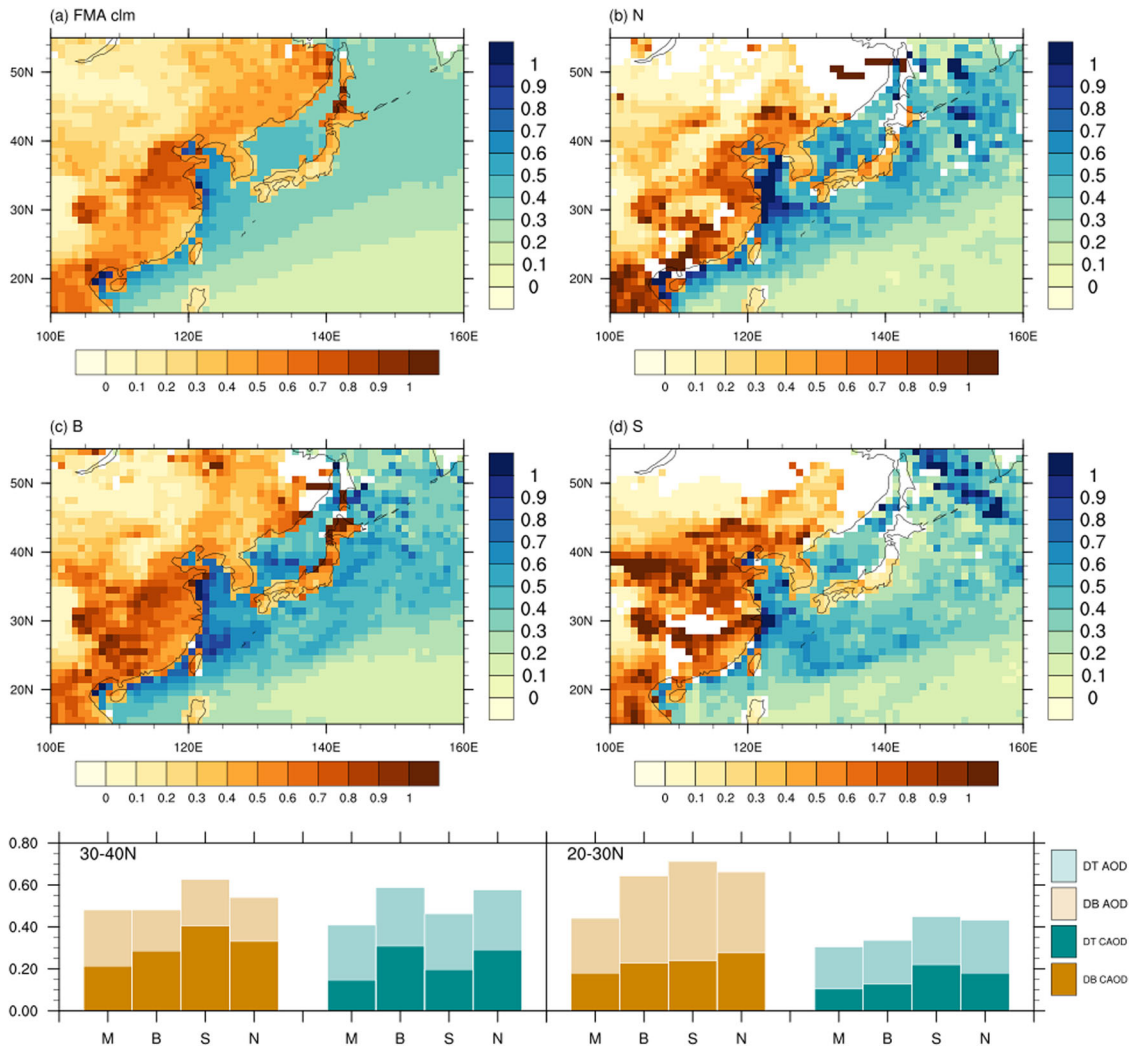
Fig. 9   The composites of AOD for PM$_{10}$ concurrent exceedance date. a The long-term mean of AOD in spring season. The composites of AOD for **b** northern, **c** broad, and **d** southern pathways. The AOD over lands are derived from Deep Blue (DB) AOD, and AOD over oceans are from Dark Target (DT) AOD. The bottom panel depicts the area-averaged AOD for regions 30°–40°N, 110°–150°E and 20°–30°N, 110°–150°E. These are overlapping bar charts. M represents the long-term mean in spring, whereas B, S, and N denote broad, southern, and northern pathways, respectively. The paler colors denote the total AOD from Deep Blue and Dart Target products. The darker colors denote the coarse-mode AOD (CAOD) components in DB AOD and DT AOD ("Methods").
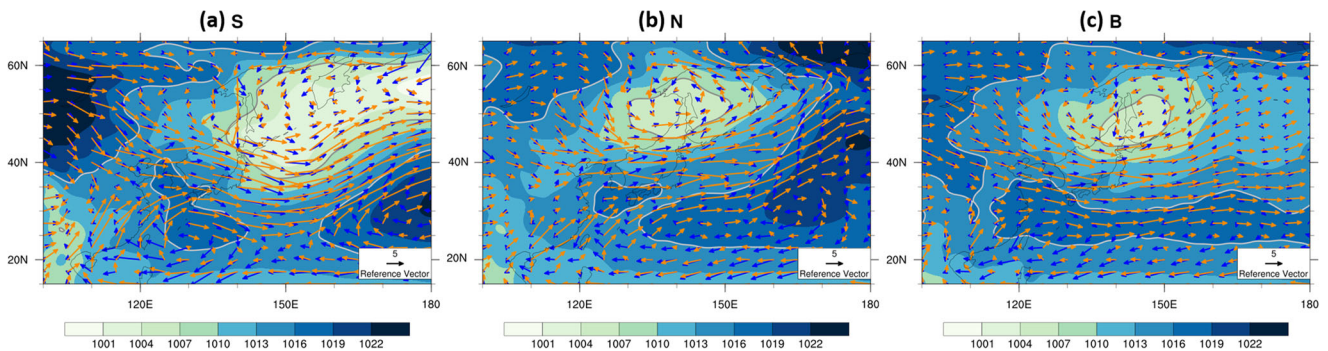

Fig. 10   The composites of mean sea level pressure and winds for PM$_{10}$ concurrent exceedance date. The composites of mean sea level pressure (shading; hPa), 10-m winds (blue vector; m s^{-1}) and 850-hPa winds (orange vector; m s^{-1}) for **a** southern, **b** northern, and **c** broad pathways. Two contour lines, 1016 hPa and 1007 hPa, are plotted for reference.

Our research revealed a lower occurrence of PM exceedance during El Niño compared to La Niña in spring. The analyzed period primarily displayed a negative PDO phase, which is favorable for the enhanced negative relationship between ENSO and East Asian winter monsoon, potentially influencing the intensity of continental outflow. Consequently, it is crucial to conduct further investigations employing comparable analyses during a positive PDO phase to gain a comprehensive understanding of ENSO-related PM exceedance in these outflow regions.

The dust-related temporal distribution exhibits a strong resemblance to the spring dust activity observed in the source regions, indicating a significant influence of dust emission on the outflow regions. In the first half of our study period (the 2000s), we observed a fluctuating sub-period characterized by several notable peaks amid a gradual decline in dust activity within the source regions over the past four decades. The increased frequency of dust outbreaks in the Asian dust source regions from the 1990s to the 2000s has been attributed to changes in aeolian erosivity and erodibility factors[51]. Aeolian erosivity, primarily driven by wind patterns, is associated with short-term extratropical cyclone activities[28,34,35], while long-term variations are linked to large-scale climate variability. The negative PDO phase has been consistently linked to a northward shift of both storm tracks and jet streams over the North Pacific; irrespective of ENSO conditions[52]. Investigating the potential connection between PDO-related changes in baroclinic activity over the North Pacific and the variability of continental weather regimes is an important issue for future research.

Aeolian erodibility is influenced by various factors, including soil and land surface properties. Both natural and anthropogenic drivers contribute to the changes in these properties. In this regard, climate change phenomena, such as Arctic amplification and sea ice variability, can also have an impact on dust variability. The previous study of Liu et al.[53] showed that the long-term decline in spring dust occurrences over northern China since the mid-1980s could be attributed to Arctic amplification, which led to weakened temperature gradients and decreased zonal winds in the preceding winter. In contrast, Fan et al.[54] suggested that the decrease in winter sea ice and snow cover could create favorable conditions for increased spring dust frequency in northern China since the mid-1990s. Nonetheless, both studies uncovered evidence of climate change's impact on Asian duct activity. Additionally, we place emphasis on investigating the pathway of dust transport to the Arctic. A previous study by Huang et al.[27] highlighted that approximately 25.2% of the Asian dust events in the 2000s could be transported to the Arctic. Moreover, a separate study by Zhao et al.[29] estimated that around 76% of the Asian dust events during the period of 2011–2015 could migrate to the Arctic. However, the precise impact of long-range dust transport on the regional climate of the Arctic remains uncertain. Understanding the long-term variations in Asian dust transport is crucial for comprehending the environmental effects of dust in regions stretching from East Asia to the Arctic.

Our results have implications for the assessment of multi-decade model simulations. While numerical simulations have provided valuable insights into the physical and chemical processes of PM variability in the Asian outflow regions during short periods or specific events[5–7,11,14,15], challenges persist in simulating long-term trends and variability of combustion aerosol and dust in the outflow region[55] and the Asian dust source regions[56]. The performance of the models is influenced by various factors, including meteorological conditions, emission sources, transport mechanisms, and modeling techniques. To effectively evaluate these models, it is crucial to use appropriate and targeted metrics that can isolate climate variability from modeling techniques. Our approach to identifying coherent patterns is simple yet effectively linked to their driving factors. In this regard,

we propose the use of the coherent patterns of PM exceedance linked to ENSO and Asian Dust as suitable metrics for targeted assessment of multi-decade model simulations in the Asian outflow regions.

METHODS

Data

The datasets used in this study are outlined in Table 1. We used multiple sources of ground-level $PM_{2.5}$ and PM_{10} concentrations. The gridded surface $PM_{2.5}$ data obtained from the Atmospheric Composition Analysis Group[2] are consistently termed as the satellite-based $PM_{2.5}$ estimates throughout this article. We derived the daily average concentrations of $PM_{2.5}$ and PM_{10} from the hourly ground-based measurements. We chose not to modify the missing value since our exceedance identification relies on daily occurrences. Thus, any missing value was considered as indicating "non-exceedance". Due to its larger number of monitoring sites and longer records, PM_{10} measurements play a crucial role in the analysis of coherent patterns. To analyze coherence, we used the daily means of selected stations in Taiwan and Hong Kong. Out of Taiwan's 77 stations, we chose 68 with over 90% data availability. Among them, 34 met these criteria: $PM_{2.5} > 30$ μg m^{-3} and $PM_{10} > 60$ μg m^{-3} averages. These stations are in central and southwestern Taiwan, called sTW (Fig. 11). The remaining 34, with lower $PM_{2.5}$ and PM_{10}, are in northern and eastern Taiwan, called nTW. In Hong Kong, 14 out of 18 stations were included in the analysis, while 2 stations were excluded due to their observational periods being less than 5 years. The locations of the Hong Kong stations can be found in the insert maps of Fig. 1b, c. For simplicity, we refer to the mean values of multiple stations in Taiwan and Hong Kong as measurements from monitoring sites throughout this article. The ground-based measurements from South Korea were not considered for the coherence analysis since their daily measurements only spanned a short period, ranging from 2 to 3 years.

Standardization and exceedance frequency

Standardization of the data is performed by calculating daily standardized anomalies for each site. Daily standardized anomalies are calculated by dividing the anomalies by the standard deviation (SD), where the anomalies represent deviations of daily PM levels from the climatological mean level across a chosen reference period. In this case, the reference period spans from 2000/2001 to 2019/2020 (cold season, from November to April). We have compared a small set of thresholds, namely one, two, and three standardized anomalies, for all the data (shown in Fig. 3). The occurrence of days exceeding the defined threshold was then counted for each station individually. These counts were subsequently used as indicators of exceedance frequency, representing the number of days in which PM levels exceed the defined threshold. For Taiwan and Hong Kong, the mean values of daily PM levels from the selected 34 and 14 stations, respectively, were used for the calculation of exceedance frequencies. To examine the representativeness of the mean values of the selected stations in Taiwan and Hong Kong, another set of exceedance frequencies was calculated by using the number of stations exceeding 1SD as thresholds. The thresholds are 9, 18, 27, and 32 stations for Taiwan, and 4, 8, 12, and 14 stations for Hong Kong (Fig. 3). The numbers of 18 and 8 stations are slightly above half of their total numbers of stations used. The climatological mean levels and the standard deviations are outlined in Supplementary Table 1. For all the monitoring sites, the climatological mean levels plus one SD (AVG+SD) for both $PM_{2.5}$ and PM_{10} closely correspond to their respective 85th percentile values. In the case of Japanese sites, the AVG+SD values for PM_{10} predominantly exceed the 90th

Table 1. Summary of the datasets used in this study.

Dataset	Parameters	Source and reference
ACAG	Monthly $PM_{2.5}$ from 1998 to 2021 Asian grids at a resolution of $0.01° \times 0.01°$	Washington University Atmospheric Composition Analysis Group[2] https://sites.wustl.edu/acag/datasets/surface-pm2-5/
TW-EPA	Hourly $PM_{2.5}$ from 2005 to 2021 Hourly PM_{10} from 1994 to 2021 Number of sites: 68 out of 77	Taiwan Environmental Protection Administration https://airtw.epa.gov.tw/ENG/default.aspx
HK-EPD	Hourly $PM_{2.5}$ from 1999 to 2021 Hourly PM_{10} from 1992 to 2021 Number of sites: 14 out of 18	Hong Kong Environmental Protection Department https://www.aqhi.gov.hk/en.html
EANET	Japan (JPA): 8 sites, hourly $PM_{2.5}$ and PM_{10} Korea (KRA): 3 sites, monthly $PM_{2.5}$ and PM_{10} China (CNA): 1 site, daily PM_{10} Time range: 2000 to 2020	Acid Deposition Monitoring Network in East Asia https://www.eanet.asia/
REASv3	Annual emissions of $PM_{2.5}$ and PM_{10} in Asia Time range: 2010 to 2015	Table 3 in ref. [1]
EPA EM	Annual emissions of $PM_{2.5}$ and PM_{10} in Taiwan Time range: 2007 to 2021	Taiwan Environmental Protection Administration https://airtw.epa.gov.tw/ENG/default.aspx
SYNOP	Dust report from 2001 to 2015 764 sites	Taiwan Central Weather Administration https://www.cwa.gov.tw/eng/
ONI	Three monthly mean of anomalous SST anomalies in the Niño 3.4 region Time range: 1950 to 2021	NOAA Climate Prediction Center (CPC) https://origin.cpc.ncep.noaa.gov/products/analysis_monitoring/ensostuff/ONI_v5.php
PDO	Monthly PDO index Time range: 1950 to 2021	NOAA National Centers for Environmental Information https://www.ncei.noaa.gov/access/monitoring/pdo/
NCEP/CFSR	Daily wind fields at 850-hPa Global grids at a resolution of $0.5° \times 0.5°$ Time range: 1979 to 2020	NOAA NCEP Climate Forecast System Reanalysis (CFSR) Accessed from the NCAR Research Data Archive https://rda.ucar.edu/datasets/ds093.0/ https://rda.ucar.edu/datasets/ds094.0/
CMORPH	Daily precipitation rate Global grids at a resolution of $0.25° \times 0.25°$ Time range: 1998–2020	CPC MORPHing technique High resolution precipitation https://www.ncei.noaa.gov/products/climate-data-records/precipitation-cmorph
MODIS [Terra]	Collection 6.1 Level-3 daily and monthly global product Global grids at a resolution of $1° \times 1°$ Time range: 2000–2021	The Level-1 and Atmosphere Archive & Distribution System Distributed Active Archive Center https://ladsweb.modaps.eosdis.nasa.gov/missions-and-measurements/science-domain/l3-atmosphere/

percentile values (Supplementary Table 1). For the identification of coherence, we used one standardized anomaly (1SD) to ensure adequate samples for analysis.

ENSO event and proportion of exceedance frequency

The smoothed ONI values, which is the 5-month running mean of the original ONI, that exceed the thresholds of $+0.5$ and $-0.5°C$ are identified as El Niño and La Niña, respectively. From the winter seasons spanning 2000/2001 to 2019/2020, a total of 7 El Niño and 7 La Niña events were identified. The El Niño events are: 2002/2003, 2004/2005, 2006/2007, 2009/2010, 2014/2015, 2015/2016, and 2018/2019 cold season. The La Niña events are: 2000/2001, 2005/2006, 2007/2008, 2008/2009, 2010/2011, 2011/2012,2017/2018 cold season. For each site, the proportion of PM exceedance is calculated as the ratio of the number of exceedance days to non-exceedance days during both El Niño and La Niña events. The same sets of El Niño and La Niña events were used for the calculations of winter (November to January) and spring (February to April) seasons. Because of the declining trends observed in some of our study sites over the past decade, we conducted an analysis of the proportion of PM exceedance using two sets of detrended time series: one with quadratic detrending and one with linear detrending. Both sets of results reveal subtle differences when compared to the non-detrended (original) time series. In this article, we present the results for the non-detrended data (refer to Fig. 7). The results for two detrended time series are shown in Supplementary Fig. 6. The values of the proportions, p-

values, and data availability in the calculation of non-detrended data are outlined in Supplementary Table 2.

Dust association

We have two steps: (1) identifying the dates of simultaneous occurrences of PM_{10} exceedance among the studied sites, and (2) associating the simultaneous occurrence dates with Asian dust events. The identification of simultaneous occurrences has been explained in the main text (refer to Fig. 8). As a result, a total of 47 dates were identified where PM_{10} exceedances occurred simultaneously across various sites. We conducted additional analyses for the simultaneous occurrences during winter and spring (Supplementary Fig. 7), which revealed similar signatures as those highlighted in Fig. 8a, but with much smaller counts for the Japanese sites in winter. We focused on extreme cases, specifically when 6, 6, and at least 9 sites simultaneously exceeded PM_{10} levels in the northern, southern, and all 12-site groups, respectively. For the all 12-site group, we termed them as the broad group. In the northern or southern group, instances where 8 sites exhibited concurrent exceedances were considered part of the broad group. Please refer to Fig. 8b for a visual representation of the results.

In order to establish the connection between specific dates and dust activity, we employed a combination of data from the dust weather visual report and existing literature. The following procedures were followed:
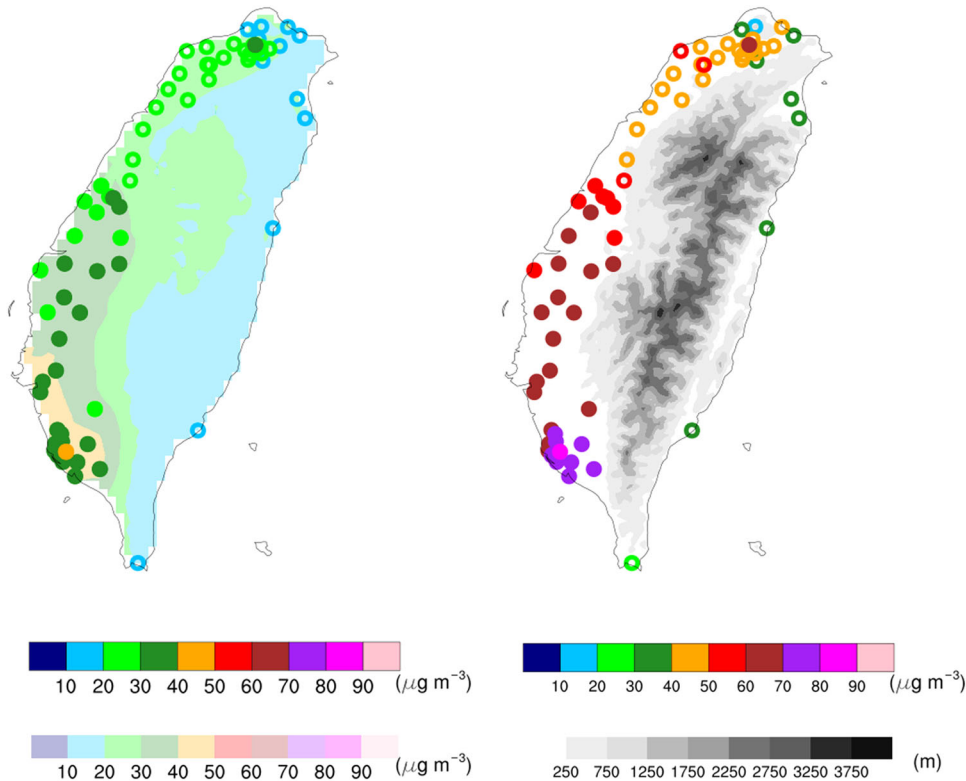
Fig. 11 Locations of Taiwanese stations and climatological averages of PM concentrations (μg m^{-3}). PM$_{2.5}$ (left) and PM$_{10}$ (right) from ground-based measurements (circles and dots) with satellite-based estimates (color shading; left) and topography (gray shading; right). The colors of circles and dots represent the climatological averages. Hollow and solid circles indicate the 34 selected stations of nTW and sTW, respectively, used for analysis of coherence.

1. We collected dust weather reports from available weather stations within our studied domain (90°–150°E, 20°–55°N) for the 47 dates of interest, as well as the 5 days prior to each date.

2. The weather stations were then mapped onto a regular 1° × 1° grid without interpolation. We identified the grid cells that contained at least one weather station as active cells. A total of 392 active cells were selected for the dust association. Our goal is to identify daily dust weather with a more extensive geographical impact. By mapping these stations onto a grid, we can treat grid cells with a high density of stations similarly to those with only 1–2 stations, thus preventing situations where a search for weather codes meeting dust weather conditions across the stations yields numerous suitable stations in close proximity to each other.

3. The selected active cells were categorized into continental and oceanic groups. For each date of concurrent exceedance, we processed the dust codes from the station(s) within each active cell to determine a daily dusty level. A dusty cell is defined as having a daily dust code of 6 or higher; the dust code of 6 denotes widespread dust in suspension in the air as defined in the World Meteorological Organization's SYNOP codes.

4. A date is deemed "dust-related" when the number of dusty cells exceeds specified thresholds. In essence, this means having a minimum of 10 dusty cells on the given date, and/or a minimum of 10 dusty cells in the preceding 4 days.

5. Subsequently, we cross-referenced these dust-related dates with previously documented dust event dates in existing literature.

The supplementary materials (Supplementary Fig. 8 and Supplementary Table 3) provide further details regarding these procedures and include the list of the 47 dates under investigation. As a result, we were able to confirm that 44 out of the 47 dates examined were associated with dust-related phenomena. Furthermore, we also used satellite-derived coarse-mode dominated AOD as a complementary assessment to reveal the geographical extent of these dates (see below).

Dust aerosol optical depth proxy

We use two sets of AOD data from the MODIS Level 3 product: one retrieved over land using the Deep Blue algorithm and the other over the ocean using the Dark Target algorithm. Both daily and monthly aerosol products retrieved by MODIS onboard the Terra satellite are used.

The Deep Blue product provides the parameter Ångström exponent, which has been demonstrated to exhibit high sensitivity to particle size[57]. We separate the coarse-mode dominated AOD by incorporating the total AOD and Ångström exponent (α) using an empirical formula based on ground-based data[58]: AOD $\times (0.98 - 0.5089\alpha + 0.0512\alpha^2)$. This coarse-mode AOD serves as a suitable proxy for representing the cumulative impact of extinction attributable to mineral particles in the atmosphere[49]. The Ångström exponent is not available within the Dark Target product. Therefore, we use the coarse-mode AOD (having effective radius $>1.0\,\mu m$[59],) from Level 3 product to represent coarse particles over the ocean. We refer to these coarse-mode AOD values, derived from both the Deep Blue and Dark Target algorithms, as CAOD for simplicity.

Out of the 47 simultaneous occurrence dates, 43 provide MODIS daily AOD data for analysis. We computed area-averaged values for daily CAOD using both the Deep Blue and Dark Target algorithms for the two regions, as depicted in Fig. 9. We examined the deviations of these area-averaged values with respect to their
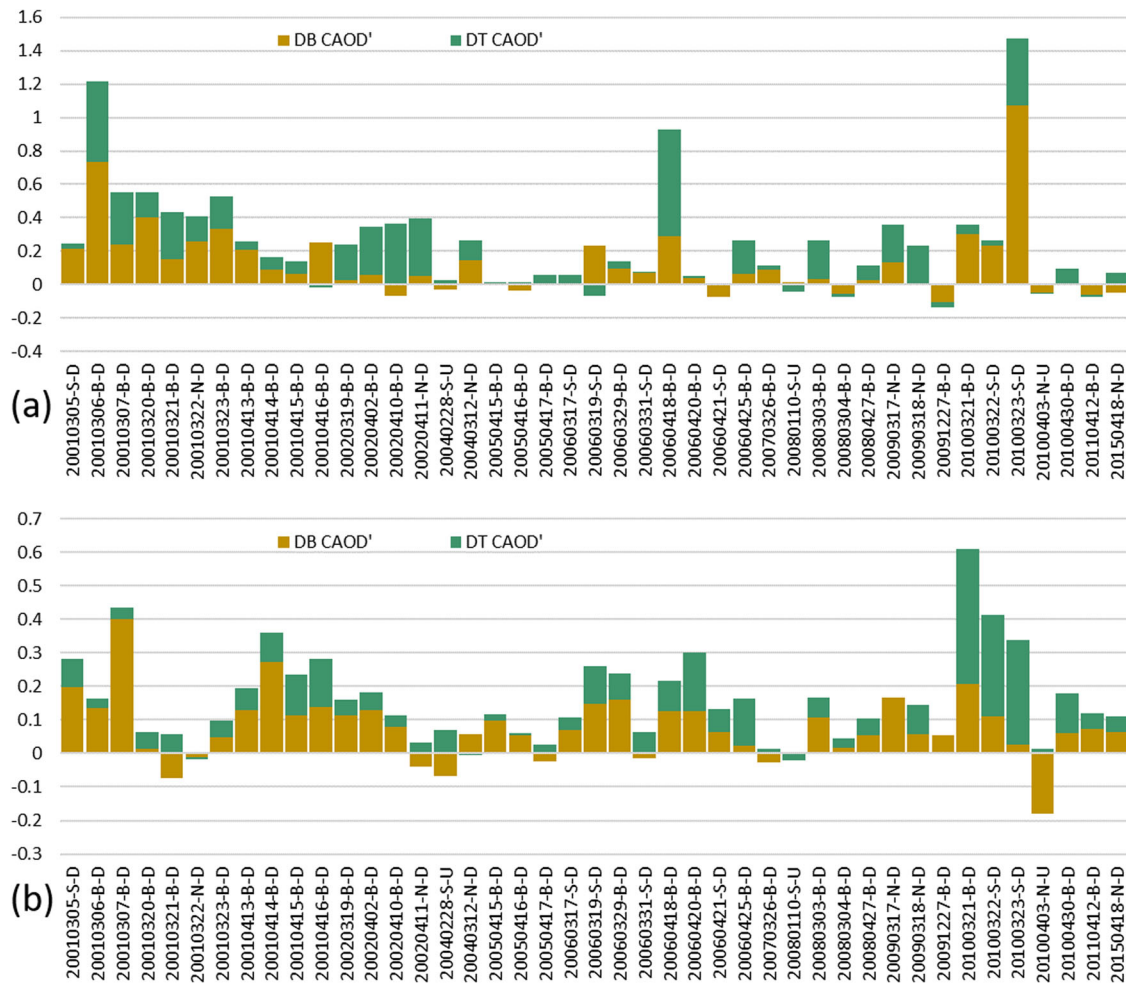
Fig. 12 The daily area-averaged coarse-mode AOD deviations for PM$_{10}$ concurrent exceedance date. The area-averaged CAOD deviations for regions **a** 30°–40°N, 110°–150°E and **b** 20°–30°N, 110°–150°E. The deviation is calculated with respect to the long-term mean of CAOD in spring season from 2001 to 2021. The Deep Blue (DB) and Dark Target (DT) CAOD' are derived for land and ocean points, respectively, within the calculation domain. Note that shown here are stacked bar charts. On the X-axis labels, the dates are displayed with a suffix that represents their respective types, where B, S, and N are the three groups as in Fig. 8 based on PM$_{10}$ concurrent exceedance, whereas D and U denote the dust-related and undetermined based on dust codes and the literature.

long-term means (Fig. 12). To assess these deviations (CAOD'), we applied two conditions: they must exceed their long-term mean values in both regions, or they must exceed their long-term mean values in at least one region. Among these dates, 21 exhibited CAOD' values exceeding their long-term mean in both regions, while 19 dates saw CAOD' exceed their long-term mean in one region. Notably, 3 dates failed to meet any of these conditions, and they were also indeterminate based on dust codes and the literature. The remaining 4 dates without available MODIS daily AOD data for analysis could be identified as dust-related using dust codes and cross-referenced to dust event dates in existing literature.

DATA AVAILABILITY
The availability of the datasets used in this study is outlined in Table 1.

CODE AVAILABILITY
Please contact the corresponding author.

REFERENCES
1. Kurokawa, J. & Ohara, T. Long-term historical trends in air pollutant emissions in Asia: Regional Emission inventory in ASia (REAS) version 3. *Atmos. Chem. Phys.* **20**, 12761–12793 (2020).
2. van Donkelaar, A. et al. Monthly global estimates of fine particulate matter and their uncertainty. *Environ. Sci. Technol.* **55**, 15287–15300 (2021).
3. Aikawa, M. et al. Significant geographic gradients in particulate sulfate over Japan determined from multiple-site measurements and a chemical transport model: impacts of transboundary pollution from the Asian continent. *Atmos. Environ.* **44**, 381–391 (2010).
4. Jeong, G. Y. Mineralogy and geochemistry of Asian dust: dependence on migration path, fractionation, and reactions with polluted air. *Atmos. Chem. Phys.* **20**, 7411–7428 (2020).
5. Kim, K.-M. et al. Modeling Asian dust storms using WRF-Chem during the DRAGON-Asia field campaign in April 2012. *J. Geophys. Res.* **126**, e2021JD034793 (2021).
6. Kumar, N. et al. Contributions of international sources to PM$_{2.5}$ in South Korea. *Atmos. Environ.* **261**, 118542 (2021).
7. Yim, S. H. L., Gu, Y., Shapiro, M. A. & Stephens, B. Air quality and acid deposition impacts of local emissions and transboundary air pollution in Japan and South Korea. *Atmos. Chem. Phys.* **19**, 13309–13323 (2019).
8. Boreddy, S. K. R. & Kawamura, K. A 12-year observation of water-soluble ions in TSP aerosols collected at a remote marine location in the western North Pacific: an outflow region of Asian dust. *Atmos. Chem. Phys.* **15**, 6437–6453 (2015).

9. Chicas, S. D. et al. Spatiotemporal distribution, trend, forecast, and influencing factors of transboundary and local air pollutants in Nagasaki Prefecture, Japan. *Sci. Rep.* **13**, 851 (2023).

10. Moreno, T. et al. Daily and hourly chemical impact of springtime transboundary aerosols on Japanese air quality. *Atmos. Chem. Phys.* **13**, 1411–1424 (2013).

11. Sugimoto, N. et al. Analysis of dust events in 2008 and 2009 using the lidar network, surface observations and the CFORS model. *Asia-Pac. J. Atmos. Sci.* **49**, 27–39 (2013).

12. Chou, C. C.-K. et al. Seasonality of the mass concentration and chemical composition of aerosols around an urbanized basin in East Asia. *J. Geophys. Res.* **122**, 2026–2042 (2017).

13. Li, T.-C. et al. Clustered longrange transport routes and potential sources of $PM_{2.5}$ and their chemical characteristics around the Taiwan Strait. *Atmos. Environ.* **148**, 152–166 (2017).

14. Lin, C.-Y. et al. The impact of channel effect on Asian dust transport dynamics: a case in southeastern Asia. *Atmos. Chem. Phys.* **12**, 271–285 (2012).

15. Lin, C.-Y. et al. Impact of different transport mechanisms of Asian dust and anthropogenic pollutants to Taiwan. *Atmos. Environ.* **60**, 403–418 (2012).

16. Liu, C.-M., Young, C.-Y. & Lee, Y.-C. Influence of Asian dust storms on air quality in Taiwan. *Sci. Total Environ.* **368**, 884–897 (2006).

17. Lee, Y. C., Yang, X. & Wenig, M. Transport of dusts from East Asian and non-East Asian sources to Hong Kong during dust storm related events 1996-2007. *Atmos. Environ.* **44**, 3728–3738 (2010).

18. Luo, M., Hou, X., Gu, Y., Lau, N. C. & Yim, S. H. L. Trans-boundary air pollution in a city under various atmospheric conditions. *Sci. Total Environ.* **618**, 132–141 (2018).

19. Yim, S. H. L., Hou, X., Guo, J. & Yang, Y. Contribution of local emissions and transboundary air pollution to air quality in Hong Kong during El Nino-Southern Oscillation and heatwaves. *Atmos. Res.* **218**, 50–58 (2019).

20. Cheng, J. et al. Dominant role of emission reduction in $PM_{2.5}$ air quality improvement in Beijing during 2013–2017: a model-based decomposition analysis. *Atmos. Chem. Phys.* **19**, 6125–6146 (2019).

21. Zheng, B. et al. Trends in China's anthropogenic emissions since 2010 as the consequence of clean air actions. *Atmos. Chem. Phys.* **18**, 14095–14111 (2018).

22. Kim, Y. P. & Lee, G. Trend of air quality in Seoul: policy and science. *Aerosol Air Qual. Res.* **18**, 2141–2156 (2018).

23. Cheng, F. Y. & Hsu, C. H. Long-term variations in $PM_{2.5}$ concentrations under changing meteorological conditions in Taiwan. *Sci. Rep.* **9**, 6635 (2019).

24. Ito, A., Wakamatsu, S., Morikawa, T. & Kobayashi, S. 30 years of air quality trends in Japan. *Atmosphere* **12**, 1072 (2021).

25. Kim, H. C. et al. Recent increase of surface particulate matter concentrations in the Seoul Metropolitan Area, Korea. *Sci. Rep.* **7**, 4710 (2017).

26. Kim, Y., Yi, S. M. & Heo, J. Fifteen-year trends in carbon species and $PM_{2.5}$ in Seoul, South Korea (2003–2017). *Chemosphere* **261**, 127750 (2020).

27. Huang, Z. et al. Short-cut transport path for Asian dust directly to the Arctic: a case study. *Environ. Res. Lett.* **10**, 114018 (2015).

28. Mao, R., Ho, C. H., Shao, Y., Gong, D. Y. & Kim, J. Infuence of Arctic oscillation on dust activity over northeast Asia. *Atmos. Environ.* **45**, 326–337 (2011).

29. Zhao, X., Huang, K., Fu, J. S. & Abdullaev, S. F. Long-range transport of Asian dust to the Arctic: identification of transport pathways, evolution of aerosol optical properties, and impact assessment on surface albedo changes. *Atmos. Chem. Phys.* **22**, 10389–10407 (2022).

30. Fan, B. et al. Earlier vegetation green-up has reduced spring dust storms. *Sci. Rep.* **4**, 6749 (2014).

31. Hara, Y., Uno, I. & Wang, Z. Long-term variation of Asian dust and related climate factors. *Atmos. Environ.* **40**, 6730–6740 (2006).

32. Song, H., Zhang, K., Piao, S. & Wan, S. Spatial and temporal variations of spring dust emissions in northern China over the last 30 years. *Atmos. Environ.* **126**, 117–127 (2016).

33. Wu, C., Lin, Z., Shao, Y., Liu, X. & Li, Y. Drivers of recent decline in dust activity over East Asia. *Nat. Commun.* **13**, 7105 (2022).

34. An, L. et al. Temporal and spatial variations in sand and dust storm events in East Asia from 2007–2016: relationships with surface conditions and climate change. *Sci. Total Environ.* **633**, 452–462 (2018).

35. Takemi, T. & Seino, N. Dust storms and cyclone tracks over the arid regions in east Asia in spring. *J. Geophys. Res.* **110**, D18S11 (2005).

36. Lee, Y. G. et al. The effects of ENSO under negative AO phase on spring dust activity over northern China: an observational investigation. *Int. J. Climatol.* **35**, 935–947 (2015).

37. Li, J., Garshick, E., Huang, S. & Koutrakis, P. Impacts of El Nino-Southern Oscillation on surface dust levels across the world during 1982–2019. *Sci. Total Environ.* **769**, 144566 (2021).

38. Bai, D., Liu, L., Dong, Z., Ma, K. & Huo, Y. Variations and possible causes of the December $PM_{2.5}$ in Eastern China during 2000–2020. *Front. Environ. Sci.* **11**, 1134940 (2023).

39. Chang, L. Y., Xu, J. M., Tie, X. X. & Wu, J. B. Impact of the 2015 El Nino event on winter air quality in China. *Sci. Rep.* **6**, 34275 (2016).

40. Sun, J. et al. Modulation of the ENSO on winter aerosol pollution in the eastern region of China. *J. Geophys. Res. Atmos.* **123**, 11–952 (2018).

41. Wang, C.-Y., Chen, J.-P. & Wang, W.-C. Meteorology-driven $PM_{2.5}$ interannual variability over East Asia. *Sci. Total Environ.* **904**, 166911 (2023).

42. Wie, J. & Moon, B. K. ENSO-related PM_{10} variability on the Korean Peninsula. *Atmos. Environ.* **167**, 426–433 (2017).

43. Son, H. Y., Park, J. Y., Kug, J. S., Yoo, J. & Kim, C. H. Winter precipitation variability over Korean Peninsula associated with ENSO. *Clim. Dyn.* **42**, 3171–3186 (2014).

44. Wang, B., Wu, R. G. & Fu, X. H. Pacific-East Asian teleconnection: how does ENSO affect East Asian climate? *J. Clim.* **13**, 1517–1536 (2000).

45. Shi, J. Reexamining the decadal variation in the ENSO-East Asian winter monsoon relationship. *Geophys. Res. Lett.* **48**, e2021GL094208 (2021).

46. Chen, C.-S. & Chen, Y.-L. The rainfall characteristics of Taiwan. *Mon. Weather Rev.* **131**, 1323–1341 (2003).

47. Chun, Y., Cho, H.-K., Chung, H.-S. & Lee, M. Historical records of Asian dust events (Hwangsa) in Korea. *Bull. Am. Meteorol. Soc.* **89**, 823–828 (2008).

48. Zhang, Y., Cai, Y. J., Yu, F., Luo, G. & Chou, C. C. K. Seasonal variations and long-term trend of mineral dust aerosols over the Taiwan region. *Aerosol Air Qual. Res.* **21**, 200433 (2021).

49. Pu, B. & Ginoux, P. How reliable are CMIP5 models in simulating dust optical depth? *Atmos. Chem. Phys.* **18**, 12491–12510 (2018).

50. Tsai, F., Chen, G. T. J., Liu, T. H., Lin, W. D. & Tu, J. Y. Characterizing the transport pathways of Asian dust. *J. Geophys. Res.* **113**, D17311 (2008).

51. Kurosaki, Y., Shinoda, M. & Mikami, M. What caused a recent increase in dust outbreaks over East Asia? *Geophys. Res. Lett.* **38**, L11702 (2011).

52. Sung, M.-K., An, S.-I., Kim, B.-M. & Woo, S.-H. A physical mechanism of the precipitation dipole in the western United States based on PDO-storm track relationship. *Geophys. Res. Lett.* **41**, 4719–4726 (2014).

53. Liu, J. et al. Impact of Arctic amplification on declining spring dust events in East Asia. *Clim. Dyn.* **54**, 1913–1935 (2020).

54. Fan, K., Xie, Z., Wang, H., Xu, Z. & Liu, J. Frequency of spring dust weather in North China linked to sea ice variability in the Barents Sea. *Clim. Dyn.* **51**, 4439–4450 (2018).

55. Yu, H. et al. Interannual variability and trends of combustion aerosol and dust in major continental outflows revealed by MODIS retrievals and CAM5 simulations during 2003–2017. *Atmos. Chem. Phys.* **20**, 139–161 (2020).

56. Wu, C. et al. Can climate models reproduce the decadal change of dust aerosol in East Asia? *Geophys. Res. Lett.* **45**, 9953–9962 (2018).

57. Eck, T. F. et al. Wavelength dependence of the optical depth of biomass burning, urban, and desert dust aerosols. *J. Geophys. Res. Atmos.* **104**, 31333–31349 (1999).

58. Anderson, T. L. et al. Testing the MODIS satellite retrieval of aerosol fine-mode fraction. *J. Geophys. Res.* **110**, 1–16 (2005).

59. Levy, R. C. et al. The Collection 6 MODIS aerosol products over land and ocean. *Atmos. Meas. Tech.* **6**, 2989–3034 (2013).

AUTHOR CONTRIBUTIONS

M.K. and C.L. initiated the research. M.K and Y.C. conducted the analyses. M.K., Y.C., and C.L. interpreted the results. M.K. drafted the manuscript with input from C.L. All authors read and approved the final manuscript.

COMPETING INTERESTS

The authors declare no competing interests.

ADDITIONAL INFORMATION

Supplementary information The online version contains supplementary material available at https://doi.org/10.1038/s41612-023-00530-z.

Correspondence and requests for materials should be addressed to Chuan-Yao Lin.

Reprints and permission information is available at http://www.nature.com/reprints

Publisher's note Springer Nature remains neutral with regard to jurisdictional claims in published maps and institutional affiliations.